CrystEngComm



PAPER

View Article Online



Cite this: CrystEngComm, 2024, 26, 1261

Received 16th November 2023, Accepted 29th January 2024

DOI: 10.1039/d3ce01153d

rsc.li/crystengcomm

Scaffold-directed growth of metal halide perovskite hopper crystals†

Qintian Zhou, a Min-Woo Kim, Yuze Zhang, b Aida Alaei, a Alexander G. Shtukenberg, Da Dilhan M. Kalyon Db and Stephanie S. Lee D**

Here we present a solution-based method of growing three-dimensional flower-shaped metal halide perovskite crystals by drop casting solutions of $FA_xMA_{1-x}Pb_vI_{1+2v}$ precursors (FA = formamidinium, MA = methylammonium) on close-packed monolayers of titanium dioxide (TiO₂) colloidal particles. The colloidal films directed perovskite crystallization during solvent evaporation, with crystals first nucleating within the confining interstitial sites between colloidal particles and growing perpendicular to the substrate surface. When growth proceeded above the colloidal film, the crystals blossomed outwards to form flower-shaped hopper crystals with a hierarchical 3D structure. The crystal shapes ranging from circular discs to pointed snowflakes were achieved by varying the solution pH and precursor composition. Structural complexity in these crystals was observed across multiple length scales - X-ray diffraction patterns and spatially-resolved photoluminescence mapping revealed three polymorphs present for all compositions tested: two bulk phases and one surface phase. These structures exhibit broad areas for light absorption but small contact areas with the underlying substrate for charge transport, which may be useful for optoelectronic devices, such as 2D photodetectors.

1. Introduction

Prescribing the sizes, shapes, and orientations of 3D microstructures with complex morphologies is being actively explored for a wide range of emerging applications, from biomaterials to catalysis and nanoelectromechanical devices.^{1,2} Recent advances in 3D printing and lithographic patterning have enabled the design and fabrication of intricate three-dimensional shapes, including spirals, tetrapods and grids, with unique photonic, mechanical and electrical properties.^{3,4} Alternatively, spontaneous, far-fromequilibrium crystallization presents a bottom-up strategy to form hierarchical microstructures. When crystallization occurs near thermodynamic equilibrium, crystal shapes are generally determined by the unit cell symmetry and relative surface energies of the crystal faces, with high surface energy faces presenting small areas on the crystal surface. To form complex 3D crystal shapes with features present at different length scales, native crystal growth habits can be disrupted by, for example, the presence of molecular additives, chemical gradients, and physical confinement. Non-equilibrium crystalline structures ranging from urchin-like spheres to ivylike vines have been reported for both inorganic compounds, such as Ga₂O₃, 5,6 BiOI, SiO₂, ZnO, 9,10 MoS₂, 11,12 and TiO₂, ^{13,14} and molecular compounds, such as L-cystine, ¹⁵ diperfluorohexylquaterthiophene (DFH-4T)¹⁶ and perylene.¹⁷

In the emerging class of optoelectronically-active metal halide perovskites, control over crystal microstructure is being investigated for applications including solar energy harvesting, 18-20 sensing, 21,22 and optics. 23,24 These materials with the chemical structure ABX3 exhibit large absorption coefficients and charge mobilities. They are also soluble in common solvents, which will enable large-scale, highthroughput manufacturing. While the majority of the literature has focused on conventional crystal shapes, such as one-dimensional wires, two-dimensional plates, and threedimensional cubes,25 top-down methods have been used to pattern metal halide perovskite films into arbitrary shapes.²⁶ Five-point perovskite stars, for example, were patterned by a combination of electron beam lithography and inductively coupled plasma etching.27 Recently, perovskite crystals with complex microstructures were formed by converting carbonate-silica microstructures grown in dynamic chemical gradients²⁸ to methylammonium lead halides through sequential ion exchange.²⁹ Complex 3D microstructures were retained during the conversion process, resulting in spiral,

^a Molecular Design Institute, Department of Chemistry, New York University, New York, NY, USA. E-mail: stephlee@nyu.edu

^b Department of Chemical Engineering and Materials Science, Stevens Institute of Technology, Hoboken, NI, USA

[†] Electronic supplementary information (ESI) available. See DOI: https://doi.org/ 10.1039/d3ce01153d

Here, we fabricate free-standing perovskite single crystals with tunable 3D flower shapes using nanoconfining scaffolds to guide the early stages of crystal growth. Specifically, perovskite precursor solutions were drop cast onto selfassembled monolayers of 600 nm-diameter TiO2 colloids and subsequently annealed to induce perovskite crystallization. The resulting crystals possess unique flower-shaped morphologies with distinct stems growing vertically from the TiO₂ scaffold followed by lateral growth outwards into petals. This scaffold-directed growth into an unconventional microstructure resembles our previous work in the growth of T-shaped perylene crystals from the cylindrical nanopores of anodized aluminum oxide.17 In the scaffold-directed growth of metal halide perovskite crystals, shapes and crystalline phases were sensitive to the deposition conditions and perovskite composition. These results demonstrate scaffolddirected crystallization combined with composition control as a strategy to fabricate complex perovskite crystal microstructures.

2. Experimental methods

TiO₂ colloidal particle synthesis

 ${
m TiO_2}$ colloidal particles were synthesized based on the procedure described by Shunsuke Tanaka. First, 95.2 mL of methanol (Pharmco, Greenfield Global USA Inc., HPLC grade) was mixed with 46.6 mL of acetonitrile (Pharmco, Greenfield Global USA Inc., HPLC grade). Then, 0.526 g of dodecylamine (DDA, Sigma-Aldrich, 98%) was added to the mixture, followed by 47.5 μ L of water. Subsequently, 1 mL of titanium tetraisopropoxide (TTIP, Sigma-Aldrich, 97%) was added to the mixture under vigorous stirring to initiate the reaction. The reaction proceeded for 16 hours. The resulting product was isolated from the suspension by centrifugation and then washed with methanol. The ${
m TiO_2}$ colloidal particles were then suspended in methanol for storage.

Compact TiO₂ layer deposition

Glass substrates with an area of 1 cm 2 were exposed to UV-ozone for 10 minutes. 0.77 mL of TTIP was added to 5 mL of ethanol with 70 mL of 30% (v/v) of HCl. Subsequently, this solution was spin-coated onto cleaned glass substrates at 2000 rpm for 30 s. The coated substrates were then annealed at 120 °C for 5 min, followed by annealing at 140 °C for 30 min. Finally, the substrates were calcined at 450 °C for 5 h in an oven.

TiO₂ colloidal monolayer deposition

 ${
m TiO_2}$ colloidal particles were first suspended in water by centrifuging and washing with deionized water to achieve a concentration of ${\sim}3.2$ g L $^{-1}$. A mixture of 1 mL of the ${
m TiO_2}$ colloidal suspension and 11 mL of deionized water was introduced into a hydrophobic plastic vial measuring 3.2 cm

in diameter and 1.5 cm in height. Next, 70 μ L of 1-pentanol (Sigma-Aldrich, 99%) was added to the solution, inducing TiO₂ colloid assembly into a monolayer at the pentanol-water interface. This monolayer was subsequently transferred onto a UV ozone-treated compact TiO₂ film on glass. Finally, the substrates were calcined at 450 °C for 5 h in an oven. The colloidal monolayer was characterized using X-ray diffraction (XRD; Bruker AXS D8 Discover GADDS microdiffractometer with Cu-K α source) and Raman spectroscopy (Thermo ScientificTM DXR3 Raman Microscope) to confirm the presence of the anatase phase, as shown in Fig. S1.†

Perovskite film deposition

FAI (formamidinium iodide, Greatcell Solar Australia Pty Ltd.)/MAI (methylammonium iodide, Greatcell Solar Australia Pty Ltd.) and PbI₂ powders (lead iodide, Tokyo Chemical Industry Co. Ltd., 99.99% trace metal basis) were added to 1 mL of DMF (N,N-dimethylformamide, Sigma-Aldrich, 99.8% anhydrous) in a stoichiometric ratio to achieve a total concentration of 1 mol L⁻¹. The solution was stirred at 70 °C for 16 hours to completely dissolve the powder. 15 μ L of solution was drop cast onto a TiO₂ colloidal monolayer or compact TiO₂ layer on glass that was pre-heated to 100 °C. The samples were held at 100 °C for 1 h to completely evaporate the solvent. All steps were performed in a N₂ environment.

X-ray diffraction analysis

Grazing-incidence wide-angle X-ray scattering (GIWAXS) patterns were collected at Brookhaven National Laboratory on Beamline 11-BM with an incident beam energy of 13.5 keV. Patterns were collected at incident X-ray angles of 0.10, 0.12, 0.15, 0.20, and 0.25°. XRD patterns collected at an incident angle of 12° were measured using a Bruker AXS D8 Discover GADDS microdiffractometer with Cu-K α source and a wavelength of 1.5406 Å. Patterns were collected at ambient temperature.

Micro-photoluminescence (μPL) spectroscopy

Local solid-state photoluminescence spectra were measured using a CRAIC 508PV microspectrophotometer (μ PL) attached to a Zeiss AXIOSKOP 40 microscope at room temperature using an aperture size of 10 μ m and an excitation wavelength of 546 nm. Measurements were done at ambient temperature.

3. Results and discussion

Perovskite crystallization upon TiO2 scaffold

 ${
m TiO_2}$ spherical colloid ($d_{
m p}=600\,{
m nm}$) monolayers assembled at an oil/water interface³¹ and transferred onto glass substrates arranged in clusters of ~8–40 close-packed colloids separated by ~300 nm gaps. FAI, MAI and PbI₂ codissolved in DMF at different molar ratios to achieve 1 M ${
m FA}_x{
m MA}_{1-x}{
m Pb}_y{
m I}_{1+2y}$ solutions with x ranging from 0 to 1 and y

CrystEngComm Paper

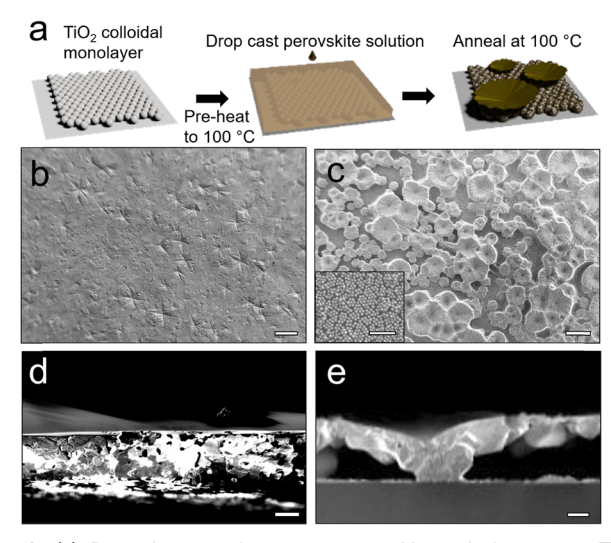


Fig. 1 (a) Procedure to drop cast perovskite solutions onto TiO₂ colloidal monolayers to form flower-shaped crystals. SEM images of FA_{0.5}MA_{0.5}PbI₃ films drop cast onto (b) a flat compact TiO₂ layer and (c) a TiO_2 colloidal monolayer film. Scale bar = 100 μ m. Inset in c displays an SEM image of a TiO2 colloidal monolayer before FA05- $MA_{0.5}PbI_3$ deposition. Scale bar = 5 μ m. (d) and (e) Cross-sectional SEM images of FA_{0.5}MA_{0.5}Pbl₃ films deposited on a compact TiO₂ layer and TiO_2 colloidal monolayer, respectively. Scale bar = 10 μ m.

ranging from 0.8 to 1 were drop casted onto TiO2 colloidal monolayers and held at 100 °C for one hour to completely evaporate the solvent (Fig. 1a). Fig. 1b and c display representative FA_{0.5}MA_{0.5}PbI₃ films deposited on a compact TiO₂ layer and a TiO₂ colloidal monolayer, respectively. As observed in previous reports, 32-36 perovskites drop cast on flat surfaces, such as compact TiO2, form a continuous polycrystalline film with $\sim 100 \mu m$ -wide individual grains impinging on one another. Each grain has a depression in the center, representing the nucleus. In contrast, the film drop cast on the TiO2 colloidal monolayer exhibited flowershaped crystals resembling morning glories. The crystals exhibited an average diameter of 60 ± 30 µm and were uniformly distributed across the substrate, with the exception of areas near the edges. Similar to perovskite grains deposited on compact TiO2, these crystals all exhibit a depression point at their centers. However, the flower-shaped crystals appear to grow elevated above the substrate surface. Cross-sectional SEM images confirm that FA_{0.5}MA_{0.5}PbI₃ grains deposited on compact TiO₂ form a dense layer coating the substrate (Fig. 1d) while those deposited on a TiO2 colloidal monolayer grow outwards above the scaffold surface from a central stem (Fig. 1e).

the difference in perovskite crystal morphologies between those grown on flat substrates versus TiO₂ colloidal monolayers to be a consequence of nanoconfined crystallization within the latter substrate. Close-packed monolayers of 600 nm-diameter TiO2 colloids have interstitial vacancies with diameters of ~220 nm. The growth of perovskite crystals that nucleate within these interstitial spaces will be constricted vertically until the crystals reach the scaffold surface. Above the scaffold surface,

the crystals are free to grow in their unconstrained morphology, resulting in fast crystallization parallel to the substrate surface to form flower-shaped structures. In situ optical microscopy images collected during drop casting are displayed in Fig. S2.† At t = 0 s, defined as the time point when the first crystals were observed, the crystal stems appear to form in the TiO2 scaffold. With increasing time for solvent evaporation, the crystals grew into flower shapes within the first four seconds. Smaller crystals also formed at the TiO2 scaffold surface, with solvent evaporation and perovskite crystallization complete after ~10 s.

Microstructure dependence on acid concentration

Hydrochloric acid (HCl) was added to precursor solutions at concentrations ranging from 0 to 10⁻³ M to examine the role of nucleation density on crystallization. In the presence of HCl above 90 °C, DMF reversibly protonates to form dimethyl ammonium and formic acid.³⁷ This reaction reduces the solubility of the perovskite precursor, resulting in an increase in perovskite crystal nucleation density with increasing HCl concentration during drop casting. Fig. 2a displays top and cross-sectional SEM images of FA_{0.5}MA_{0.5}PbI₃ flower-shaped crystals grown from TiO2 scaffolds in the presence of HCl. For HCl concentrations ranging from 0 to 10⁻⁴ M, the crystal nucleation density remained constant at ~ 54 nuclei per um², corresponding to an average crystal diameter of 110 \pm 50 μm At the highest HCl concentration of 10⁻³ M, on the other hand, the nucleation density increased to 180 nuclei per mm², resulting in a smaller average crystal diameter of 50 ± 20 μm.

Cross-sectional SEM images also revealed that the crystal stems decrease in height with increasing HCl concentration (Fig. 2b). Decreased stem heights indicate an earlier transition from vertical to horizontal growth during solvent evaporation. We expect this trend in stem height to result from differences in time-dependent solute concentration profiles during drop casting. As the concentration of HCl increases, nucleation densities also rise, which accelerates the depletion of solute during film formation. This rapid solute consumption hastens the transition to diffusion-limited crystallization. In this growth regime, solute molecules preferentially attach to crystal edges to form the flower petals.

Microstructure dependence on perovskite composition

The role of the FA+: MA+ ratio on the flower-shaped perovskite crystallization was also quantified. SEM images of perovskite crystals drop cast on TiO2 colloidal monolayers for different compositions of FAxMA1-xPbI3 displayed in Fig. 3 revealed flower shapes to vary from circular for $MAPbI_3$ (x =0) to hexagonal for FAPbI₃ (x = 1). FA_{0.75}MA_{0.25}PbI₃ crystals adopt a star-like shape with round vertices and slightly concave edges. Increasing the FA⁺ content slightly to FA_{0.8}MA_{0.2}PbI₃ resulted in a more pronounced hexagonal symmetry. FAPbI₃ crystals were regular hexagons, reflecting the trigonal P3m1 symmetry of α -FAPbI₃.

Paper CrystEngComm

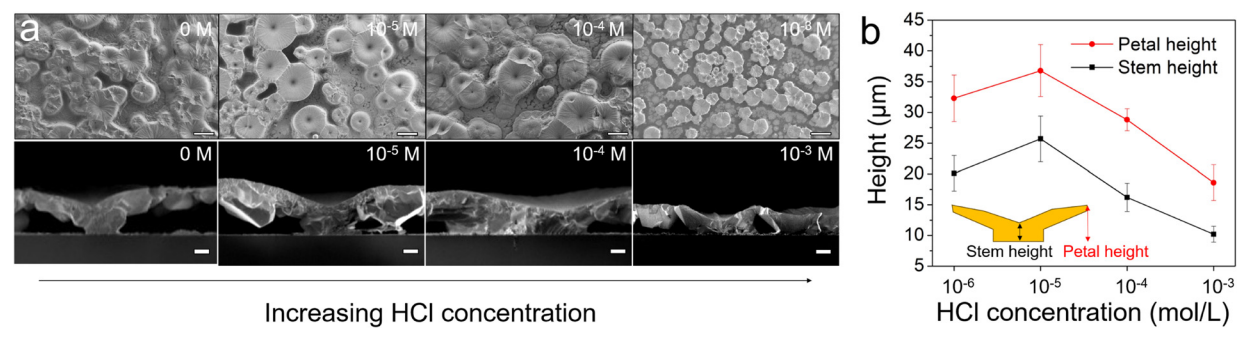


Fig. 2 (a) Top view (top row) and cross-sectional (bottom row) SEM images of FA_{0.5}MA_{0.5}PbI₃ flower-shaped crystals grown in the presence of HCl (HCl concentration is indicated in the upper right corners of images). Scale bars on top and bottom rows are 100 and 10 μm, respectively. (b) FA_{0.5}MA_{0.5}Pbl₃ flower and stem heights versus precursor solution pH.

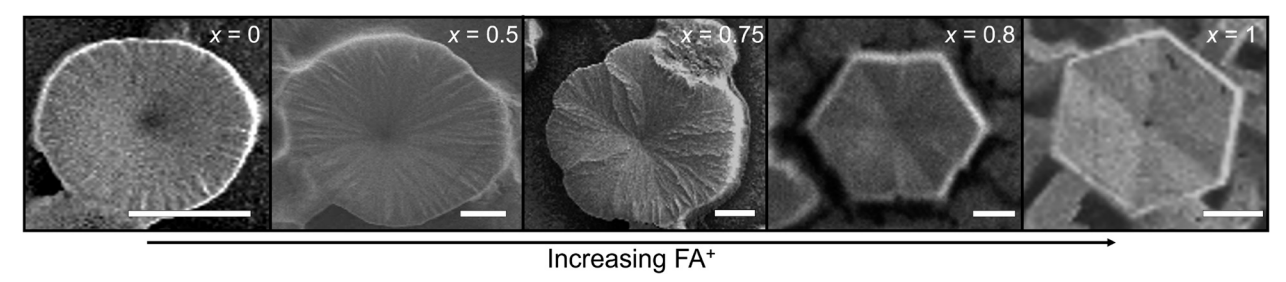


Fig. 3 SEM images of $FA_xMA_{1-x}PbI_3$ perovskite flower-shaped crystals in which x was varied from 0 to 1. Scale bar = 30 μ m.

These crystals appear to be single crystalline, with the upper face parallel to the substrate surface corresponding to the (100) plane as previously observed in films crystallized from solution at temperatures between 90 °C to 150 °C.33 These results suggest that crystals confined within the TiO2 scaffold first grow upwards along the $\langle 100 \rangle$ direction. Once the crystals grow above the scaffold surface, fast growth occurs in all directions perpendicular to the \langle 100 \rangle direction, resulting in a flowershaped morphology. While all crystals expose the (100) plane parallel to the substrate surface, the crystal morphology differs depending on the FA+: MA+ ratio. Pure MAPbI₃ adopts the cubic α-phase during crystallization at 100 °C. Some crystal branching occurs during growth, resulting in the formation of circular crystals (Fig. 3, leftmost panel). This morphology has been previously reported in MAPbI3 films, but without vertical growth. α-FAPbI₃, on the other hand, has a trigonal crystal structure resulting in hexagonal crystals with well-defined corners and edges.³⁸ For compositions comprising mixtures of MA⁺ and FA⁺, the crystals adopt intermediate morphologies progressing from circular to hexagonal with increasing FA+ content. These intermediate compositions all adopt a cubic crystal symmetry.39

Crystal morphology is determined not only by the composition-dependent crystal symmetry, but also by the stoichiometry. Fig. 4 displays SEM images of perovskite crystals with different FA+: MA+ ratios grown in PbI2-poor solution ranging from 0.95 to 0.85 times the stoichiometric amount. For all compositions, crystal edges develop depressions in the middle, with the depression increasing with decreasing PbI₂ concentration. MAPbI₃ crystals retain their

overall circular shape, but the boundaries became significantly rougher with the appearance of many distinct protruding vertices (Fig. 4a-c). For FA⁺-rich compositions (Fig. 4d-i), straight edges developed progressively larger depressions with decreasing PbI2 concentration. Crystal surface roughening was also observed. Lower magnification SEM images of the crystals are included in Fig. S3.†

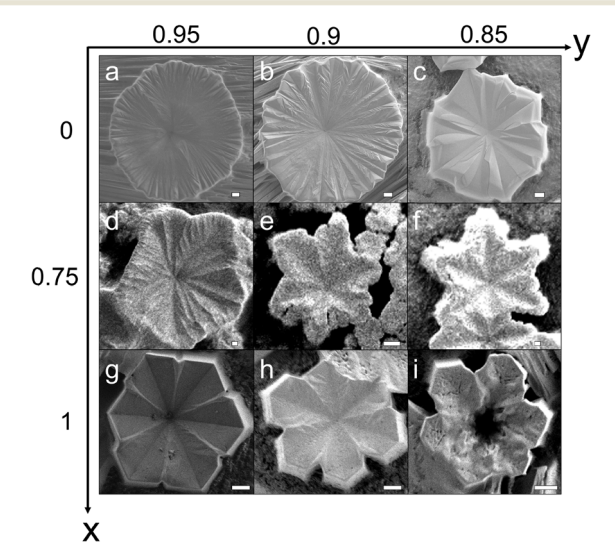


Fig. 4 SEM images of $FA_xMA_{1-x}Pb_yI_{1+2y}$ flower-shaped crystals for the following compositions: (a) $FAPb_{0.95}I_{2.9}$, (b) $FAPb_{0.9}I_{2.8}$, (c) $\mathsf{FAPb}_{0.85}\mathsf{I}_{2.7}, \quad \text{(d)} \quad \mathsf{FA}_{0.75}\mathsf{MA}_{0.25}\mathsf{Pb}_{0.95}\mathsf{I}_{2.9}, \quad \text{(e)} \quad \mathsf{FA}_{0.75}\mathsf{MA}_{0.25}\mathsf{Pb}_{0.9}\mathsf{I}_{2.8}, \quad \text{(f)}$ $\mathsf{FA}_{0.75}\mathsf{MA}_{0.25}\mathsf{Pb}_{0.85}\mathsf{I}_{2.7}, \quad \text{(g)} \quad \mathsf{MAPb}_{0.95}\mathsf{I}_{2.9}, \quad \text{(h)} \quad \mathsf{MAPb}_{0.9}\mathsf{I}_{2.8}, \quad \mathsf{and} \quad \text{(i)}$ $MAPb_{0.85}I_{2.7}$. Scale bar = 10 μ m.

Edge roughening likely occurs due to a shift to a diffusion-controlled growth regime. Perovskite crystals adopt faces with straight edges in interface-controlled or mixed regimes when the material supply is fast enough to maintain a high concentration of all components everywhere along the growth front. Once the material supply becomes insufficient, the growth regime shifts toward diffusion-controlled growth, which is accompanied by planar growth front instability and dendritic growth. In this case, enough material can be supplied only at the edge vertices.

Polymorphism in flower-shaped crystals

Grazing incidence wide-angle X-ray scattering (GIWAXS) patterns were collected on perovskite films deposited on TiO2 colloidal monolayers for FA⁺ ratios ranging from 0 to 1 (Fig. S2a-j†). Multiple crystalline phases were observed for all samples. Two sets of peaks in the diffraction pattern collected on MAPbI₃ crystals were indexed to α - and β -MAPbI₃ (α -MAPbI₃ space group: Pm3m, ICSD no: 7236651; β-MAPbI₃ space group: I4cm, ICSD no: 7218931), labelled with * and #, respectively, in Fig. 5a. These sets of peaks shifted systematically to lower q values with increasing FA+ content, consistent with prior reports. 40-42 The diffraction patterns of FA-rich films exhibited peaks associated with both α - and δ -FAPbI₃ (α -FAPbI₃ space group: P3m1, ICSD no: 4335631; δ-FAPbI₃ space group: P6₃mc, ICSD no: 4335640) (Fig. S2j†), indicating that partial phase transition to the thermodynamically stable δ -phase occurred prior to GIWAXS measurements.

A third set of peaks in all diffraction patterns could not be indexed to any common phases of MAPbI₃ or FAPbI₃. In the diffraction pattern collected on MAPbI₃, this set of peaks matches that reported for a distorted MAPbI₃ phase (space group: $Im\bar{3}$, ICSD no: 4516749) observed in crystals pressurized to 0.7 GPa.⁴³ In this distorted phase, the Pb-I-Pb bond angle is between 145–158°, compared to 167.6° in β-MAPbI₃ and 150.5–163.5° in γ-MAPbI₃.⁴⁴ Incident angle-dependent X-ray diffraction patterns displayed in Fig. 4b in the q range of 1.993 to 2.053 Å⁻¹ (see Fig. S2a† for the entire

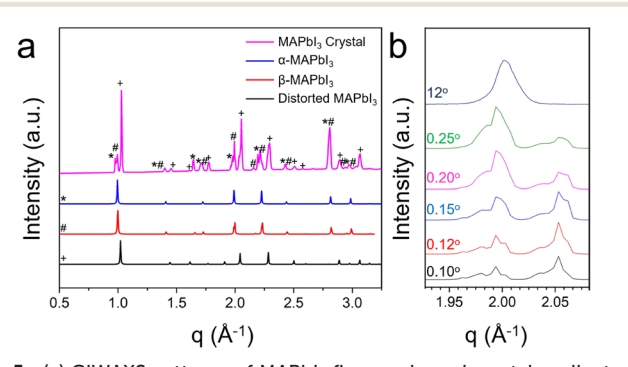


Fig. 5 (a) GIWAXS patterns of MAPbI $_3$ flower-shaped crystals collected at an X-ray incident angle of 0.10°. Simulated powder patterns of α -MAPbI $_3$ (*) and β -MAPbI $_3$ (#) and the distorted MAPbI $_3$ (+) phases are provided for comparison. (b) GIWAXS patterns highlighting the 220 reflection of β -MAPbI $_3$ and the distorted phase collected at different X-ray incident angles.

q range) revealed the ratio of peak intensities of the distorted phase $(q=2.053~\text{Å}^{-1})$ to the β -MAPbI₃ 220 reflection $(q=1.993~\text{Å}^{-1})$ to decrease with increasing X-ray penetration depth. This trend was observed across different compositions (Fig. S4†) and suggests that a distorted phase forms on perovskite crystal surfaces. When diffraction patterns were collected at a larger incident angle of 12°, peaks related to the distorted phase were not observed (Fig. 4b and S5†).

Photoluminescence (PL) spectra ($\lambda_{ex}=546$ nm) were collected on 10 × 10 μm areas of MAPbI $_3$ films using a microspectrophotometer integrated with an optical microscope (Fig. 6a). The locations include: 1) and 2) the center and edge of a flower-shaped crystal, respectively, and 3) flat perovskite crystals surrounding the crystal (Fig. 6b). PL spectra collected on the flower-shaped crystal comprised two peaks centered at 768 nm and 800 nm, as determined by Gaussian fits. In contrast, the PL spectrum collected on the flat perovskite film surrounding the flower displayed a single peak at 767 nm, corresponding to the typical emission wavelength of β -MAPbI $_3$ crystals. 38

In some reports, low energy PL peaks are attributed to the presence of large defect densities that contribute to subbandgap charge recombination. 45,46 The magnitude of the low energy peak can be decreased by passivating the defects by depositing a second compound, such as thiophene or benzothiadiazole to passivate positively and negatively charged defects, respectively, on top of the film. 45,47 In the case of MAPbI₃ flower-shaped crystals, the ratio of the peak intensities was unaffected by the presence of either compound (Fig. S6†). Another possibility is that this peak is from α-MAPbI₃ crystals, which fluoresce around 800 nm. 38,48 This hypothesis is consistent with the observation of the α-phase in GIWAXS diffraction patterns across compositions. A low energy PL peak is likewise observed across compositions, with both peaks shifting to lower energies with increasing FA⁺ content (Fig. S7†). In comparison, only a single high-energy peak at 770 nm is observed in the PL spectrum of needle-like crystals formed lower crystallization temperatures (Fig. S8†).

A PL map was constructed using an aperture of 10 μm on a 74 μm -wide MAPbI $_3$ flower-shaped crystal to estimate spatial

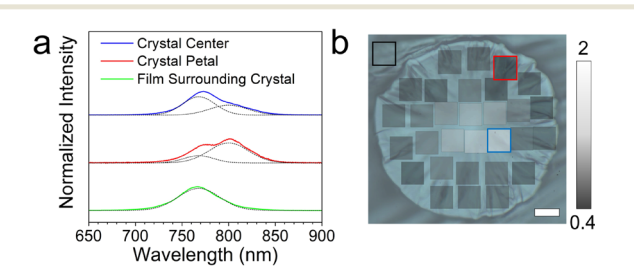


Fig. 6 (a) PL spectra of a flower-shaped crystal at different locations. Dashed curves display Gaussian fits for each spectrum. (b) Map of high- and low-energy PL peak intensity ratios on a MAPbl $_{\! 3}$ flower-shaped crystal. Scale bar = 10 μm . The squares with black, red and blue outlines correspond to locations at which the spectra in (a) were collected.

distribution of the two crystalline phases on the crystal surface. Fig. 6b displays an overlay of the locations at which PL spectra (squares approximately represent the aperture size) were collected. The color of each square indicates the ratio of highto low-energy peak intensities. Larger ratios were observed at the crystal center, while smaller ratios were observed on the surrounding petal. These results suggest that the crystal stems primarily adopt the thermodynamically stable β-phase while the petals contain a larger fraction of the α -phase. α - and β-MAPbI₃ are known to co-exist at room temperature, forming stable layered superlattices. 49 α-Phase stabilization may be entropic in nature, with methylammonium cations having more rotational freedom in the α -phase compared to the β and γ-phases,⁵⁰ or a consequence of mechanical strain.^{51,52} Polymorph selection is also sensitive to the degree of supersaturation during crystal growth from solution. 53-55 During drop casting at 100 °C, the extent of supersaturation is dynamic. At the time after drop casting the solution is undersaturated. As the solvent evaporates, the solution concentration increases. Crystal nucleation requires reaching a critical supersaturation, at which crystallization starts and material is consumed. The rate of supersaturation increase by solvent evaporation and supersaturation decrease by crystallization depends on many factors and may vary nonlinearly with time. It is conceivable that high supersaturation immediately after nucleation accompanied the formation of crystal stems and favoring β-MAPbI₃ sharply decreased upon massive crystallization favoring α -MAPbI₃ in crystal petals. The film surrounding crystals formed at the very end of crystallization when supersaturation increased significantly with evaporation of residual solvent, again favoring β-MAPbI₃.

4. Conclusions

Progressing beyond the deposition of flat, polycrystalline films to grow crystals with complex morphologies will enable new technologies that rely on spatially inhomogeneous interactions with photons and electrons. Here, hierarchical FAxMA1-xPbvI1+2v 3D structures were achieved through a combination of scaffold-guided crystallization, tuning compositions to alter crystal symmetries and controlling the crystal growth regime during solution-phase deposition. Whereas crystals grown on flat substrates tend to orient with their fast growth direction(s) parallel to the substrate surface, nanostructured scaffolds can direct crystals to grow vertically occurred Crystallization first within nanoconfining pores of the scaffold before proceeding to the open, unconfined space above the scaffold surface, resulting in inhomogeneous crystal widths perpendicular to the substrate surface. In this case, flower-shaped perovskite crystals blossom from narrow stems. These shapes exhibit broad areas for light absorption but relatively small contact areas at the perovskite/substrate interface for electron transfer. Similar structures have been used previously for directing light^{56,57} and as photonic trumpets.^{58,59} Concave microstructures can also enhance light trapping in perovskite films, leading to improved photodetector performance compared to flat films. 60,61 Based on these promising applications, we anticipate that the crystal growth mechanisms to form hierarchical perovskite crystals detailed herein will inform the development of high-performance optoelectronics.

Conflicts of interest

The authors declare no conflicts of interest.

Acknowledgements

S. S. L. acknowledges support from the National Science Foundation under Award Number CMMI-AM-1846178. D. M. K. and Y. Z. acknowledge support from the PSEG Foundation to advance energy innovation at Stevens. This research used Beamline 11-BM of the National Synchrotron Light Source II, a U.S. Department of Energy (DOE) Office of Science User Facility operated for the DOE Office of Science by Brookhaven National Laboratory under Contract No. DE-SC0012704 with the help of Dr. Ruipeng Li.

References

- 1 M. Vaezi, H. Seitz and S. F. Yang, Int. J. Adv. Manuf. Technol., 2013, 67, 1721.
- 2 C. Barner-Kowollik, M. Bastmeyer, E. Blasco, G. Delaittre, P. Muller, B. Richter and M. Wegener, *Angew. Chem., Int. Ed.*, 2017, 56, 15828.
- 3 K. L. Liu, H. B. Ding, S. Li, Y. F. Niu, Y. Zeng, J. N. Zhang, X. Du and Z. Z. Gu, *Nat. Commun.*, 2022, **13**, 4563.
- 4 R. D. Farahani, M. Dubé and D. Therriault, *Adv. Mater.*, 2016, **28**, 5794.
- 5 G. Sinha and S. Chaudhuri, *Mater. Chem. Phys.*, 2009, **114**, 644.
- 6 L. Xu, Y. Su, S. Li, Y. Q. Chen, Q. T. Zhou, S. Yin and Y. Feng, J. Phys. Chem. B, 2007, 111, 760.
- 7 K. X. Ren, K. Zhang, J. Liu, H. D. Luo, Y. B. Huang and X. B. Yu, CrystEngComm, 2012, 14, 4384.
- 8 Z. Yan, F. Zhang, J. C. Wang, F. Liu, X. L. Guo, K. W. Nan, Q. Lin, M. Y. Gao, D. Q. Xiao, Y. Shi, Y. T. Qiu, H. W. Luan, J. H. Kim, Y. Q. Wang, H. Y. Luo, M. D. Han, Y. G. Huang, Y. H. Zhang and J. A. Rogers, *Adv. Funct. Mater.*, 2016, 26, 2629.
- 9 H. Wang, Q. Li, X. K. Zheng, C. Wang, J. W. Ma, B. B. Yan, Z. N. Du, M. Y. Li, W. J. Wang and H. Q. Fan, J. Alloys Compd., 2020, 829, 154453.
- 10 B. X. Li and Y. F. Wang, J. Phys. Chem. Solids, 2011, 72, 1165.
- 11 H. B. Zhang, L. Yu, T. Chen, W. Zhou and X. W. Lou, *Adv. Funct. Mater.*, 2018, **28**, 1807086.
- 12 L. M. Yu, F. Guo, S. Liu, J. L. Qi, M. L. Yin, B. Yang, Z. Y. Liu and X. H. Fan, *Mater. Lett.*, 2016, **183**, 122.
- 13 M. Y. Wang, Y. Y. Zhu, D. Meng, K. K. Wang and C. Y. Wang, Mater. Lett., 2020, 277, 128372.
- 14 J. Wang, Y. Zhou and Z. Shao, Electrochim. Acta, 2013, 97, 386.
- 15 J. D. Rimer, Z. H. An, Z. N. Zhu, M. H. Lee, D. S. Goldfarb, J. A. Wesson and M. D. Ward, *Science*, 2010, 330, 337.

- 16 M. Yilmaz, E. Babur, M. Ozdemir, R. L. Gieseking, Y. Dede, U. Tamer, G. C. Schatz, A. Facchetti, H. Usta and G. Demirel, *Nat. Mater.*, 2017, 16, 918.
- 17 A. Alaei, K. Zong, K. Asawa, T. M. Chou, A. L. Briseno, C. H. Choi and S. S. Lee, *Soft Matter*, 2021, 17, 3603.
- 18 Y. Xiang, X. Mo, X. Li, K. Huang, P. He, G. Dai and J. Yang, J. Phys. D: Appl. Phys., 2022, 55, 073001.
- 19 N. Phung and A. Abate, Small, 2018, 14, 1802573.

CrystEngComm

- 20 L. Etgar, P. Gao, Z. S. Xue, Q. Peng, A. K. Chandiran, B. Liu, M. K. Nazeeruddin and M. Grätzel, J. Am. Chem. Soc., 2012, 134, 17396.
- 21 Y. He, I. Hadar and M. G. Kanatzidis, *Nat. Photonics*, 2022, **16**, 14.
- 22 M. Y. Cho, S. Kim, I. S. Kim, E. S. Kim, Z. J. Wang, N. Y. Kim, S. W. Kim and J. M. Oh, Adv. Funct. Mater., 2020, 30, 1907449.
- 23 J. Zhao, Y. Zhao, Y. Guo, X. Zhan, J. Feng, Y. Geng, M. Yuan, X. Fan, H. Gao, L. Jiang, Y. Yan and Y. Wu, *Adv. Funct. Mater.*, 2021, 31, 2105855.
- 24 Z. Hu, Z. Liu, Z. Zhan, T. Shi, J. Du, X. Tang and Y. Leng, *Adv. Photonics*, 2021, **3**, 034002.
- 25 Y. Fu, H. Zhu, J. Chen, M. P. Hautzinger, X. Y. Zhu and S. Jin, *Nat. Rev. Mater.*, 2019, 4, 169.
- 26 B. Jeong, H. Han and C. Park, Adv. Mater., 2020, 32, 2000597.
- 27 N. Zhang, W. Sun, S. P. Rodrigues, K. Wang, Z. Gu, S. Wang, W. Cai, S. Xiao and Q. Song, *Adv. Mater.*, 2017, 29, 1606205.
- 28 W. L. Noorduin, A. Grinthal, L. Mahadevan and J. Aizenberg, *Science*, 2013, **340**, 832.
- 29 T. Holtus, L. Helmbrecht, H. C. Hendrikse, I. Baglai, S. Meuret, G. W. P. Adhyaksa, E. C. Garnett and W. L. Noorduin, *Nat. Chem.*, 2018, 10, 740.
- 30 S. Tanaka, D. Nogami, N. Tsuda and Y. Miyake, *J. Colloid Interface Sci.*, 2009, 334, 188.
- 31 S. W. Shi and T. P. Russell, Adv. Mater., 2018, 30, 1800714.
- 32 Y. H. Li, Y. F. Zhang, Z. H. Zhao, L. L. Zhi, X. B. Cao, Y. Jia, F. Lin, L. Zhang, X. Cui and J. Q. Wei, *Cryst. Growth Des.*, 2018, 18, 3458.
- 33 C. A. T. Zuo and L. M. Ding, Angew. Chem., Int. Ed., 2021, 60, 11242.
- 34 L. Zhang, C. Zuo and L. Ding, J. Semicond., 2021, 42, 072201.
- 35 C. T. Zuo, A. D. Scully, W. L. Tan, F. Zheng, K. P. Ghiggino, D. Vak, H. Weerasinghe, C. R. McNeill, D. Angmo, A. S. R. Chesman and M. Gao, *Commun. Mater.*, 2020, 1, 33.
- 36 R. Lu, Y. Liu, J. Zhang, D. Zhao, X. Guo and C. Li, *Chem. Eng. J.*, 2022, **433**, 133845.
- 37 N. K. Noel, M. Congiu, A. J. Ramadan, S. Fearn, D. P. McMeekin, J. B. Patel, M. B. Johnston, B. Wenger and H. J. Snaith, *Joule*, 2017, 1, 328.
- 38 A. Alaei, A. Circelli, Y. H. Yuan, Y. Yang and S. S. Lee, *Mater. Adv.*, 2021, 2, 47.
- 39 M. T. Weller, O. J. Weber, J. M. Frost and A. Walsh, J. Phys. Chem. Lett., 2015, 6, 3209.
- 40 B. Slimi, M. Mollar, I. Ben Assaker, I. Kriaa, R. Chtourou and B. Mari, *Energy Procedia*, 2016, **102**, 87.

- 41 X. L. Guo, K. H. Ngai, M. C. Qin, X. H. Lu, J. B. Xu and M. Z. Long, *Nanotechnology*, 2021, 32, 075406.
- 42 Y. Huang, L. Li, Z. H. Liu, H. Y. Jiao, Y. Q. He, X. G. Wang, R. Zhu, D. Wang, J. L. Sun, Q. Chen and H. P. Zhou, J. Mater. Chem. A, 2017, 5, 8537.
- 43 A. Jaffe, Y. Lin, C. M. Beavers, J. Voss, W. L. Mao and H. I. Karunadasa, ACS Cent. Sci., 2016, 2, 201.
- 44 A. Varadwaj, P. R. Varadwaj and K. Yamashita, *ChemistrySelect*, 2018, 3, 7269.
- 45 K. Schotz, A. M. Askar, W. Peng, D. Seeberger, T. P. Gujar, M. Thelakkat, A. Kohler, S. Huettner, O. M. Bakr, K. Shankar and F. Panzer, *J. Mater. Chem. C*, 2020, 8, 2289.
- 46 A. Dobrovolsky, A. Merdasa, J. Li, K. Hirselandt, E. L. Unger and I. G. Scheblykin, *J. Phys. Chem. Lett.*, 2020, **11**, 1714.
- 47 N. K. Noel, A. Abate, S. D. Stranks, E. S. Parrott, V. M. Burlakov, A. Goriely and H. J. Snaith, *ACS Nano*, 2014, 8, 9815.
- 48 X. Q. Kong, K. Shayan, S. Lee, C. Ribeiro, S. Strauf and S. S. Lee, *Nanoscale*, 2018, **10**, 8320.
- 49 T. W. Kim, S. Uchida, T. Matsushita, L. Cojocaru, R. Jono, K. Kimura, D. Matsubara, M. Shirai, K. Ito, H. Matsumoto, T. Kondo and H. Segawa, *Adv. Mater.*, 2018, 30, 1705230.
- 50 A. Bonadio, C. A. Escanhoela, F. P. Sabino, G. Sombrio, V. G. de Paula, F. F. Ferreira, A. Janotti, G. M. Dalpian and J. A. Souza, J. Mater. Chem. A, 2021, 9, 1089.
- 51 M. Faghihnasiri, M. Izadifard and M. E. Ghazi, *J. Phys. Chem. C*, 2017, **121**, 27059.
- 52 E. G. Moloney, V. Yeddu and M. I. Saidaminov, *ACS Mater. Lett.*, 2020, 2, 1495.
- 53 N. C. S. Kee, R. B. H. Tan and R. D. Braatz, Cryst. Growth Des., 2009, 9, 3044.
- 54 J. Bernstein and O. University Press Scholarship, Polymorphism in molecular crystals, Oxford University Press, Oxford, United Kingdom; New York, NY, 2nd edn, 2020.
- 55 S. Datta and D. J. W. Grant, Cryst. Res. Technol., 2005, 40, 233.
- 56 J. H. Atwater, P. Spinelli, E. Kosten, J. Parsons, C. Van Lare, J. Van de Groep, J. G. de Abajo, A. Polman and H. A. Atwater, Appl. Phys. Lett., 2011, 99, 151113.
- 57 Y. Gao, H. Cansizoglu, K. G. Polat, S. Ghandiparsi, A. Kaya, H. H. Mamtaz, A. S. Mayet, Y. A. Wang, X. Z. Zhang, T. Yamada, E. P. Devine, A. F. Elrefaie, S. Y. Wang and M. S. Islam, *Nat. Photonics*, 2017, 11, 301.
- 58 M. Munsch, N. S. Malik, E. Dupuy, A. Delga, J. Bleuse, J. M. Gérard, J. Claudon, N. Gregersen and J. Mork, *Phys. Rev. Lett.*, 2013, 111, 239902.
- 59 P. Stepanov, A. Delga, N. Gregersen, E. Peinke, M. Munsch, J. Teissier, J. Mork, M. Richard, J. Bleuse, J. M. Gérard and J. Claudon, *Appl. Phys. Lett.*, 2015, 107, 141106.
- 60 Y. X. Zhang, Y. C. Liu, Z. Yang, M. Chen and S. Z. Liu, Adv. Funct. Mater., 2020, 30, 2002742.
- 61 W. H. Wang, Y. R. Ma and L. M. Qi, Adv. Funct. Mater., 2017, 27, 1603653.